



## Liquid phase epitaxy growth and visible emission of $\text{Tb}^{3+}, \text{Gd}^{3+}:\text{LiYF}_4$ layers

Amandine Baillard, Gurvan Brasse, Pavel Loiko, Rosa Maria Solé, Magdalena Aguiló, Francesc Díaz, Xavier Mateos, Abdelmjid Benayad, Vivien Ménard, Alain Braud, et al.

### ► To cite this version:

Amandine Baillard, Gurvan Brasse, Pavel Loiko, Rosa Maria Solé, Magdalena Aguiló, et al.. Liquid phase epitaxy growth and visible emission of  $\text{Tb}^{3+}, \text{Gd}^{3+}:\text{LiYF}_4$  layers. *Optical Materials Express*, 2023, 13 (8), pp.2355-2368. 10.1364/ome.491569 . hal-04208915

**HAL Id: hal-04208915**



**<https://hal.science/hal-04208915>**

Submitted on 15 Sep 2023

**HAL** is a multi-disciplinary open access archive for the deposit and dissemination of scientific research documents, whether they are published or not. The documents may come from teaching and research institutions in France or abroad, or from public or private research centers.

L'archive ouverte pluridisciplinaire **HAL**, est destinée au dépôt et à la diffusion de documents scientifiques de niveau recherche, publiés ou non, émanant des établissements d'enseignement et de recherche français ou étrangers, des laboratoires publics ou privés.

# Liquid phase epitaxy growth and visible emission of $\text{Tb}^{3+}$ , $\text{Gd}^{3+}$ : $\text{LiYF}_4$ layers

AMANDINE BAILLARD,<sup>1</sup> GURVAN BRASSE,<sup>1</sup> PAVEL LOIKO,<sup>1</sup> ROSA MARIA SOLÉ,<sup>2</sup>  MAGDALENA AGUILÓ,<sup>2</sup> FRANCESC DÍAZ,<sup>2</sup> XAVIER MATEOS,<sup>2,†</sup>  ABDELMJID BENAYAD,<sup>1</sup> VIVIEN MÉNARD,<sup>1</sup> ALAIN BRAUD,<sup>1</sup> AND PATRICE CAMY<sup>1,\*</sup>

<sup>1</sup>Centre de Recherche sur les Ions, les Matériaux et la Photonique (CIMAP), UMR 6252

CEA-CNRS-ENSICAEN, Université de Caen, 6 Boulevard du Maréchal Juin, 14050 Caen Cedex 4, France

<sup>2</sup>Universitat Rovira i Virgili (URV), Física i Cristal·lografia de Materials (FiCMA), Marcel·li Domingo 1, 43007 Tarragona, Spain

<sup>†</sup>Serra Hünter Fellow, Spain

\*patrice.camy@ensicaen.fr

**Abstract:** Single-crystalline layers of 12 at.%  $\text{Tb}^{3+}$ , 5 at.%  $\text{Gd}^{3+}$ : $\text{LiYF}_4$  were grown by the liquid phase epitaxy method on (001) oriented bulk undoped  $\text{LiYF}_4$  substrates using  $\text{LiF}$  as a solvent. The growth temperature was 737–740 °C, the growth duration was 15 - 25 min, and the layer thickness was 40–90  $\mu\text{m}$ . The structural, morphological, vibronic and spectroscopic properties of the layers were studied.  $\text{Tb}^{3+}$  ions were uniformly distributed in the layers with no diffusion into the substrate. Polarized Raman spectroscopy confirmed the orientation of the layers (growth along the [001] direction). Under excitation in the blue, the layers exhibited intense green emission. For the  $^5\text{D}_4 \rightarrow ^7\text{F}_5$   $\text{Tb}^{3+}$  transition, the peak stimulated-emission cross-section is  $1.28 \times 10^{-21} \text{ cm}^2$  at 542.0 nm for  $\pi$ -polarization. The luminescence lifetime of the  $^5\text{D}_4$   $\text{Tb}^{3+}$  state is 5.05 ms at room temperature. The crystal-field splitting of  $\text{Tb}^{3+}$  multiplets was determined at low temperature. The developed epitaxies are promising for green and yellow waveguide lasers.

© 2023 Optica Publishing Group under the terms of the [Optica Open Access Publishing Agreement](#)

## 1. Introduction

Trivalent terbium ions ( $\text{Tb}^{3+}$ ) possess an electronic configuration of  $[\text{Xe}]4f^8$ , with a group of lower-lying  $^7\text{F}_J$  multiplets ( $J = 0 - 6$ , where  $^7\text{F}_6$  is the ground state) and a metastable state  $^5\text{D}_4$ . The  $\text{Tb}^{3+}$  ion presents multi-color emissions in the visible due to the  $^5\text{D}_4 \rightarrow ^7\text{F}_J$  transitions, with the most intense one at ~544 nm falling into the green spectral range (the  $^5\text{D}_4 \rightarrow ^7\text{F}_5$  transition) [1]. The  $^5\text{D}_4$   $\text{Tb}^{3+}$  state does not suffer from cross-relaxation and presents a relatively long lifetime (about 5 ms for fluoride materials) even at high  $\text{Tb}^{3+}$  doping concentrations [2]. One of the difficulties for pumping terbium ions is that the transition in absorption  $^7\text{F}_6 \rightarrow ^5\text{D}_4$  is spin-forbidden, so it corresponds to very low absorption cross-section, in the order of  $10^{-22} \text{ cm}^2$ . Still, terbium ions can be efficiently excited in the UV spectral range [3].

$\text{Tb}^{3+}$ -doped materials are widely used as green phosphors [4–6], e.g., in fluorescent lamps.  $\text{Eu}^{2+}$ - and  $\text{Eu}^{3+}$ -based blue / red phosphors combined with  $\text{Tb}^{3+}$ -based ones can provide trichromatic lighting technology. Terbium is also used as a probe in biochemistry [7,8]. Note that terbium-containing crystals are also often used in magneto-optical devices, because of their large effective magnetic moment and high paramagnetic susceptibilities. Recent studies show that Faraday rotator properties can be improved by incorporating Tb [9,10].

Tetravalent  $\text{Tb}^{4+}$  ions also exist, but previous studies have shown that they do not contribute to any visible emission and just act as quenching centers, with absorption bands in the visible [11,12].

$\text{Tb}^{3+}$  ions are also suitable for generating laser emission in two distinct spectral ranges: in the mid-IR for low-phonon-energy hosts like chalcogenide glasses ( $h\nu_{\text{ph}} \sim 250 - 350 \text{ cm}^{-1}$ ), with

continuous-wave laser emission observed at 4.9 - 5.5  $\mu\text{m}$  (the  ${}^7\text{F}_5 \rightarrow {}^7\text{F}_6$  transition) [13,14], and in the visible with fluoride crystals, mainly  $\text{LiYF}_4$ , at 544 nm (green lasers) and 587 nm (yellow ones) [15–17]. Efficient lasing in the visible was difficult to obtain at first because of the low absorption cross-sections and the risk of excited-state absorption. The first significant results about a  $\text{Tb}^{3+}$  visible laser were published in 2007 [18]. Currently, the main trends for the development of visible  $\text{Tb}^{3+}$  lasers are: (i) the use of blue GaN laser diodes as pump sources, and (ii) the use of heavily doped materials for boosting the pump absorption [15]. Lasing in  $\text{Tb}^{3+}$ -based stoichiometric crystals ( $\text{LiTbF}_4$ ,  $\text{TbF}_3$ ) was also achieved [1,2].

Currently,  $\text{Tb}^{3+}$  visible lasers are based only on fluoride crystals, mainly  $\text{LiYF}_4$ , which is a well-known laser host matrix. It has a scheelite ( $\text{CaWO}_4$ ) like tetragonal structure and belongs to the  $I4_1/a$  space group. It has a broad transparency range (0.12 - 7.5  $\mu\text{m}$ ) and exhibits low phonon energy ( $h\nu_{\text{ph}} = 444 \text{ cm}^{-1}$ ).  $\text{LiYF}_4$  features good thermo-mechanical properties, *i.e.*, high thermal conductivity and weak anisotropy of thermal expansion. It has a single substitution rare-earth site ( $\text{Y}^{3+}$  site,  $S_4$  symmetry), and in the case of  $\text{Tb}^{3+}$  doping,  $\text{Li}_{1-x}\text{Tb}_x\text{F}_4$  solid-solutions exist up to 100 at.% substitution, *i.e.*, reaching the  $\text{LiTbF}_4$  stoichiometric composition [19].

Liquid Phase Epitaxy (LPE) is a well-known method for growing oriented single-crystalline layers of high optical quality which are particularly well suited for applications as planar laser waveguides [20].  $\text{LiYF}_4$  is very suitable for the LPE growth [21] and crystalline  $\text{LiYF}_4$  layers doped with various rare-earth ions such as  $\text{Tm}^{3+}$  [22],  $\text{Er}^{3+}$  [23],  $\text{Yb}^{3+}$  [24],  $\text{Ho}^{3+}$  [25] or  $\text{Pr}^{3+}$  [26] have already been elaborated by LPE, including heavily doped (20 at.%) ones [23,27,28]. In particular, visible waveguide lasers have been demonstrated employing  $\text{Pr}:\text{LiYF}_4$  epitaxial layers codoped with  $\text{Gd}^{3+}$  and  $\text{Lu}^{3+}$  buffer ions to address the green (522 nm), red (639 nm) and orange (605 nm) spectral ranges [26]. LPE is capable of producing low-loss (down to 0.14 dB/cm in the red)  $\text{LiYF}_4$ -based crystalline layers, with a thickness between a few  $\mu\text{m}$  to several hundreds of  $\mu\text{m}$ , on relatively large substrates (a few  $\text{cm}^2$ ) and with high growth rates (up to a few  $\mu\text{m}/\text{min}$ ). The stress induced at the layer / substrate interface is reduced for a homo-epitaxial growth, *i.e.*, when the layer and the substrate are of the same nature, as in the case of rare-earth-doped  $\text{LiYF}_4$  on undoped  $\text{LiYF}_4$ . So far, the growth of  $\text{Tb}^{3+}$ -doped  $\text{LiYF}_4$  epitaxial layers by LPE has never been reported.

In the present work, we report on the LPE growth and morphological, vibronic, and polarized spectroscopic properties of single-crystalline  $\text{Tb}^{3+}, \text{Gd}^{3+}$ -codoped  $\text{LiYF}_4$  epitaxial layers with the goal of developing novel active media for visible waveguide lasers.

## 2. Liquid phase epitaxy growth

Single-crystalline layers of  $\text{LiYF}_4$  codoped with  $\text{Tb}^{3+}$  and  $\text{Gd}^{3+}$  ions were grown using the LPE method on undoped bulk  $\text{LiYF}_4$  substrates. Here,  $\text{Tb}^{3+}$  ions were introduced as active optical centers responsible of the visible emission and  $\text{Gd}^{3+}$  ones (being optically passive) – to increase the refractive index contrast between the layer and the substrate for waveguide applications. The starting batch composition was 73 mol%  $\text{LiF}$  - 27 mol%  $\text{REF}_3$  ( $\text{RE} = \text{Y, Tb, Gd, rare-earth}$ ) as represented by the dashed red line on the phase diagram of the  $\text{LiF} - \text{YF}_3$  binary system [29], see Fig. 1. Lithium fluoride ( $\text{LiF}$ ) served as both the solvent and the constituent material of the  $\text{LiREF}_4$  phase. Here, the temperatures corresponding to the eutectic (E) and peritectic (P) points are 695 °C and 815 °C, respectively. To analyze the expected effect of heavy  $\text{Tb}^{3+}$  doping on the growth conditions, we also plotted the phase diagram of the  $\text{LiF} - \text{TbF}_3$  system [30] corresponding to the crystallization of the  $\text{LiTbF}_4$  stoichiometric phase. The replacement of  $\text{Y}^{3+}$  by  $\text{Tb}^{3+}$  is expected to shift both the E and P points and the liquidus curve. For the studied 73 mol%  $\text{LiF}$  - 27 mol%  $\text{REF}_3$  composition, a slightly lower (by 1-1.5 °C) onset of apparent crystallization is indeed observed in line with the phase diagrams. Note the non-congruent melting of both  $\text{LiYF}_4$  and  $\text{LiTbF}_4$  phases.

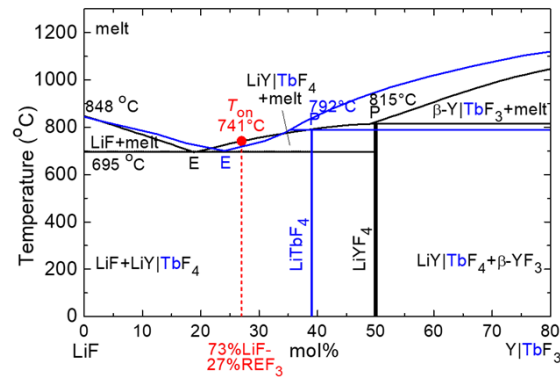


**Fig. 1.** Phase diagram of the LiF – YF<sub>3</sub> (black) and LiF – TbF<sub>3</sub> (blue) binary systems [29,30]. The dashed red line corresponds to the composition selected for the LPE growth, and red circle - to the apparent onset of crystallization.

The layers were doped with 12 at.% Tb<sup>3+</sup> and 5 at.% Gd<sup>3+</sup> (starting composition), with both ions substituting yttrium ions Y<sup>3+</sup>. Their ionic radii for VIII-fold F<sup>−</sup> coordination are  $R_{\text{Tb}} = 1.18 \text{ \AA}$ ,  $R_{\text{Gd}} = 1.19 \text{ \AA}$  and  $R_{\text{Y}} = 1.16 \text{ \AA}$  [31], respectively, being relatively close, so that the stress induced by the doping is expected to be relatively weak.

The undoped LiYF<sub>4</sub> substrates (lateral size:  $33 \times 11 \text{ mm}^2$ , thickness: 3 mm) were cut from a bulk crystal grown by the Czochralski method, oriented with their plane orthogonal to the [001] crystallographic axis, and then polished until very low surface rugosity was reached (<3 nm).

The reagents used for the LPE growth were lithium fluoride LiF (Alfa Aesar, 99.5% purity), and rare-earth oxides Y<sub>2</sub>O<sub>3</sub>, Gd<sub>2</sub>O<sub>3</sub> and Tb<sub>2</sub>O<sub>3</sub> (Alfa Aesar REaction, <99.9% purity). The oxide precursors were fluorinated to obtain rare-earth fluorides (REF<sub>3</sub>) of high purity.

The growth bath containing thoroughly mixed precursors was first placed in the LPE chamber, which was degassed to a pressure of  $2 \times 10^{-4}$  mbar at 400 °C. Then, the bath was heated to a temperature higher than the liquidus point to melt every component. After homogenizing the bath with stirring, it was slowly cooled to a temperature slightly below the apparent onset of crystallization. Lowering the temperature and introducing the substrate in the supersaturated solution started crystallization of epitaxial layers. Several growth attempts were made with the growth temperature being in the range of 737–740 °C and the growth duration of 15 - 25 min. High-quality optical layers were achieved according to the following procedure: first setting the temperature to 738 °C for 15 min, then raising it to 740 °C for 10 min, with a rotation speed of 5 rpm. The layers were grown on both sides of the substrate. After the growth was completed, the epitaxies were slowly removed from the solution and pulled up from the LPE oven with a speed of a few mm per minute.

### 3. Characterization methods

The surface morphology of non-polished epitaxial layers was observed using an optical confocal microscope (Sensofar, S-neox), in reflection mode, using a blue GaN diode (405 nm) or an UV lamp (365 nm). The layer topography was studied in the interferometric mode. Energy Dispersive X-ray (EDX) spectra and element mapping were measured with a FEI Scios 2 Field Emission Scanning Electron Microscope with a focused Gallium ion beam (FESEM-FIB).

The phases crystallized from the molten bath of the LPE growth were identified by X-ray powder diffraction (XRD). The equipment used was a Bruker-AXS D8-Advance diffractometer using Cu K $\alpha$  radiation, incident and diffracted beam Soller slits of 2.5° and a fixed receiving slit of 0.5°. The diffractograms were measured for 2 $\theta$  angles from 5° to 80°, with a step size

of  $0.02^\circ$  and a step time of 0.5 s. The detection of the diffracted X-rays was performed with a LynxEye-XE-T PSD detector with an opening angle of  $2.94^\circ$ .

The polarized  $\mu$ -Raman and  $\mu$ -luminescence spectra, as well as  $\mu$ -luminescence maps were measured at room temperature (RT, 293 K) using a confocal Raman microscope (InVia Qontor, Renishaw), equipped with a  $\times 50$  Leica objective and an  $\text{Ar}^+$  ion laser (488 / 514 nm).

The excitation / luminescence spectra and the luminescence decay curves were also measured using a spectrofluorometer (QuantaMaster, Horiba). For low-temperature (LT, 12 K) measurements, the epitaxy was mounted on a APD DE-202 cryo-cooler equipped with a APD HC-2 Helium Vacuum Cryo Compressor. The spectral bandwidth (SBW) for LT studies was 0.1–0.25 nm, depending on the spectral range.

## 4. Results and discussion

### 4.1. Layer morphology

Figure 2(a) presents a photograph of an as-grown 12 at.% Tb, 5 at.% Gd: $\text{LiYF}_4/\text{LiYF}_4$  epitaxy (growth temperature / duration:  $738^\circ\text{C}$  / 15 min, then  $740^\circ\text{C}$  / 10 min). Approximately 2/3 of the substrate was vertically dipped into the solution and the epitaxial layers were grown over the whole dipped area on both sides of the substrate. A rounded-shaped growth meniscus is easily observed. The white color of the overgrown part of the epitaxy is due to crystallization of the residual solvent (LiF). The parts of the layer free of LiF crystallization were transparent. The same sample is shown in Fig. 2(b) under illumination with a UV lamp. An intense green emission due to the  $\text{Tb}^{3+}$  ions is observed.

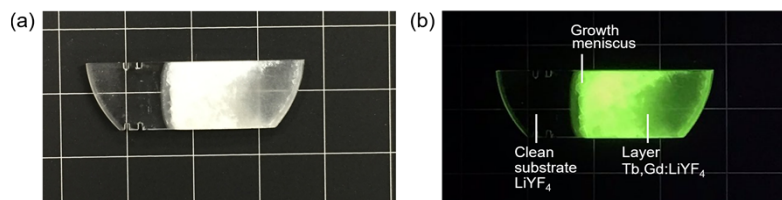


**Fig. 2.** (a) A photograph of the as-grown Tb,Gd: $\text{LiYF}_4$  /  $\text{LiYF}_4$  epitaxy (the growth temperature / duration is  $738^\circ\text{C}$  for 15 min, then  $740^\circ\text{C}$  for 10 min), (b) the same sample illuminated by a UV lamp,  $\lambda_{\text{exc}} = 365$  nm.

Confocal laser microscopy was employed to study the layer morphology, Fig. 3. Figures 3(a,b) represent the raw top surface, with “hills and valleys” topography, being typical of fluoride LPE growth. The epitaxial layer shows a smooth surface, while the crystallized residual solvent LiF presents a dendritic-like structure, Fig. 3(b). One of the lateral facets of the epitaxy was polished to observe the cross-sectional view, see Fig. 3(c). It indicates a clean and distinct interface between the substrate and the layer, with an average layer thickness of  $74 \pm 15 \mu\text{m}$ . For the performed LPE growth experiments, the layer thickness was ranging from 40 to  $90 \mu\text{m}$ , depending on the growth temperature and duration, resulting in a range of growth rates of 1.6–3.6  $\mu\text{m}/\text{min}$ . The residual solvent was easily removed from the top surface of the layer by polishing, as shown in Fig. 3(d), illustrating a final layer with a thickness of  $30 \mu\text{m}$ . Both the substrate and the layer show no cracks nor inclusions of secondary phases.

The surface topography of the as-grown top layer surface was further revealed in the interferometric mode, Fig. 4(a). The root mean square (r.m.s.) surface roughness was about  $1 \mu\text{m}$  as measured along the A-B line passing across several “hills” and “valleys”, Fig. 4(b). Note that for the substrate, the surface roughness measured in a similar way was about a few nm (after polishing).

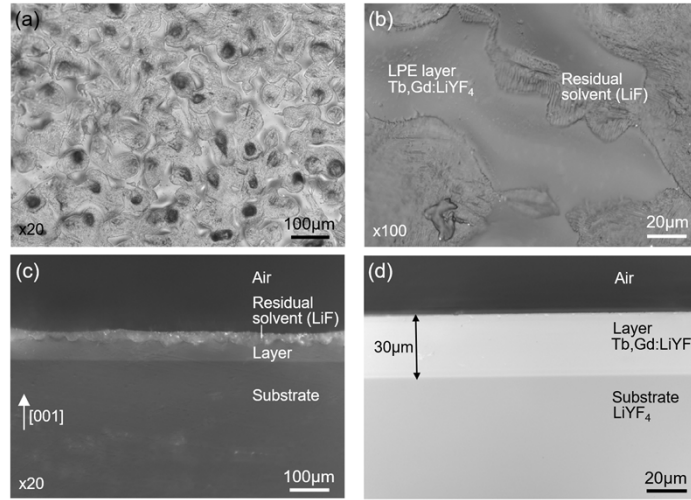


**Fig. 3.** Confocal laser microscopy images of the Tb,Gd:LiYF<sub>4</sub> epitaxial layers: (a,b) top view, raw surface; (c) side view, polished end-facet, (d) side view, top and side polished layer, reflection mode,  $\lambda = 405$  nm.

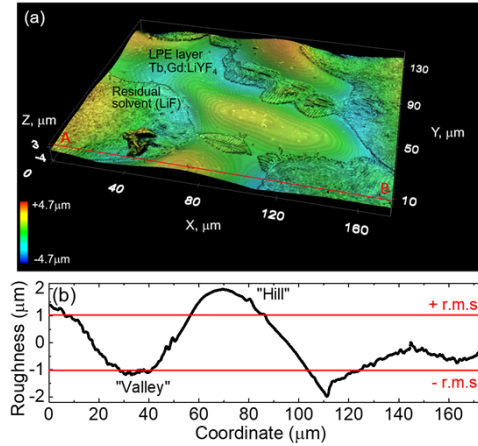


**Fig. 4.** Surface topography of the as-grown Tb,Gd:LiYF<sub>4</sub> epitaxial layer: (a) a 3D topography plot, (b) a surface roughness plot along the A – B line (r.m.s. – root mean square deviation).

#### 4.2. XRD and EDX

After the epitaxial growth, the LPE molten bath was cooled down to room temperature and the crystallized materials were studied by powder XRD, see Fig. 5. Two phases were easily separated: transparent single-crystals and a translucent polycrystalline material. The single-crystals correspond to a tetragonal (sp. gr.  $I4_1/a$ ) scheelite-type LiYF<sub>4</sub>-based phase with lattice parameters  $a = 5.1754$  Å and  $c = 10.7650$  Å. The translucent polycrystalline material is composed of the same LiYF<sub>4</sub>-based phase, as well as a small amount of LiF with a face centred cubic structure (sp. gr.  $Fm-3m$ ).

Assuming a very close composition of the single-crystals and the epitaxial layer, the lattice mismatch between the layer and the substrate could be estimated yielding  $\Delta a/a_{\text{substrate}} = 0.20\%$  and  $\Delta c/c_{\text{substrate}} = 0.22\%$ . Here, we used the lattice constants of undoped LiYF<sub>4</sub>:  $a = 5.164$  Å



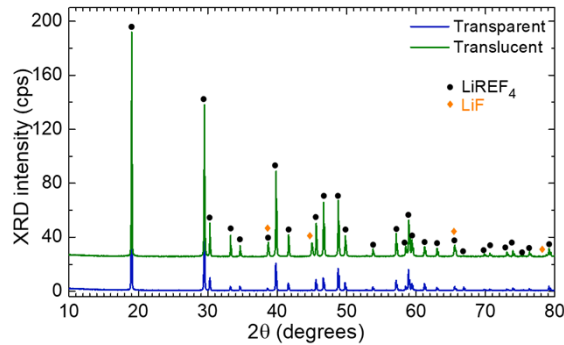


**Fig. 5.** X-ray powder diffraction (XRD) patterns of the crystallized molten bath of the LPE experiment: a translucent polycrystalline material and transparent single crystals, the assignment of the diffraction peaks is after the PDF cards No. 81-1940 ( $\text{LiYF}_4$ ) and No. 04-0857 ( $\text{LiF}$ ) from the ICDD database.

and  $c = 10.741 \text{ \AA}$  [32]. The increase in the lattice constants of the layer with respect to the substrate are due to the larger ionic radii of both  $\text{Tb}^{3+}$  and  $\text{Gd}^{3+}$  as compared to that of  $\text{Y}^{3+}$  (see above).  $\text{LiY}_{1-x-y}\text{Tb}_x\text{Gd}_y\text{F}_4$  ( $0 < x, y < 1$ ) represents a substitutional solid-solution in the  $\text{LiYF}_4$ - $\text{LiGdF}_4$ - $\text{LiTbF}_4$  ternary system, so the variation of the lattice constants can be calculated from the weighted mean of the constituents' lattice parameters (the Vegard's law). In this way, we achieved  $a_{\text{calc}} = 5.172 \text{ \AA}$  and  $c_{\text{calc}} = 10.771 \text{ \AA}$  in a relatively good agreement with the experimental measurement. Here, the following lattice constants were used:  $a = 5.203 \text{ \AA}$  and  $c = 10.879 \text{ \AA}$  ( $\text{LiTbF}_4$ ) [19] and  $a = 5.235 \text{ \AA}$  and  $c = 11.019 \text{ \AA}$  ( $\text{LiGdF}_4$ ) [33].

The composition of the epitaxial layer was studied by EDX analysis and elemental mapping. The EDX spectrum of the epitaxial layer is shown in Fig. 6(a) and indicates the presence of Y, F and Tb (Li is too light to be detected by EDX analysis). Figure 6(b) shows a FESEM image of the lateral facet of the epitaxy, exhibiting the substrate, the layer and the residual solvent LiF on top of the latter. The elemental mapping was used to reveal the element distribution in both the layer and the substrate. Figure 6(c) shows a homogenous distribution of F in the layer and the substrate, with an increase in the area assigned to the residual solvent LiF. The Y content decreases in the layer compared to the substrate, Fig. 6(d), and Tb is uniformly distributed in the layer, Fig. 6(e), substituting for Y.

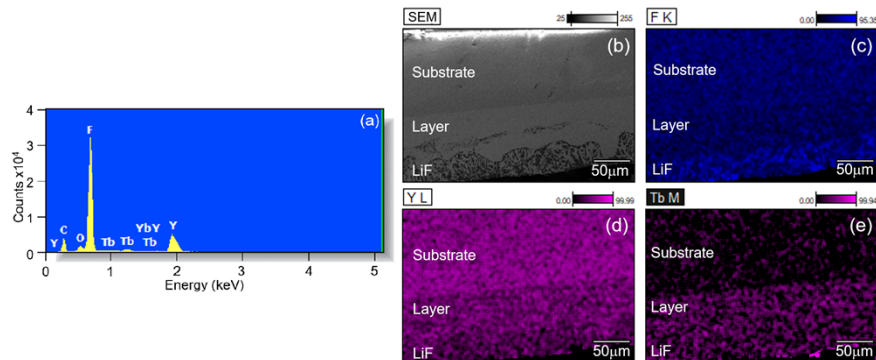


**Fig. 6.** (a) EDX spectrum of the  $\text{Tb,Gd:LiYF}_4$  epitaxial layer. (b-e) Element mapping across the polished end-facet of the epitaxy: (b) a FESEM image, (c-e) element maps: (c)  $\text{F K}\alpha_{1,2}$ , (d)  $\text{Y La1}$  and (e)  $\text{Tb Ma1}$ .

### 4.3. Raman spectra

The polarized  $\mu$ -Raman spectra of the epitaxial layer are shown in Fig. 7(a). The measures were made in the  $a(ij)a$  configuration (where  $i, j = \sigma$  or  $\pi$ , using Porto's notations for polarized Raman spectroscopy [34]) observing a polished side facet of the epitaxy with a spatial resolution better than  $1\ \mu\text{m}$ . At the center of the Brillouin zone  $\Gamma$  ( $k = 0$ ), vibrational modes are distributed over the irreducible representations of the  $C_{4h}$  point group as follows:  $3A_g + 5B_g + 5E_g + 5A_u + 3B_u + 5E_u$ . One  $A_u$  and one  $E_u$  modes correspond to rigid translations of the whole crystal, and other  $A_u$  and  $E_u$  modes are IR-active. The *gerade* (g) modes ( $5B_g + 5E_g$ ) are Raman-active and the remaining modes ( $B_u$ ) are silent. The  $a(\pi\pi)a$  configuration shows the most intense Raman peak at  $264\ \text{cm}^{-1}$ , corresponding to an  $A_g$  vibrational mode, with a full width at half maximum (FWHM) of  $8.8\ \text{cm}^{-1}$ . The highest energy vibrations are observed at  $424\ \text{cm}^{-1}$  ( $B_g$ ) and  $444\ \text{cm}^{-1}$  ( $E_g$ ) [35].

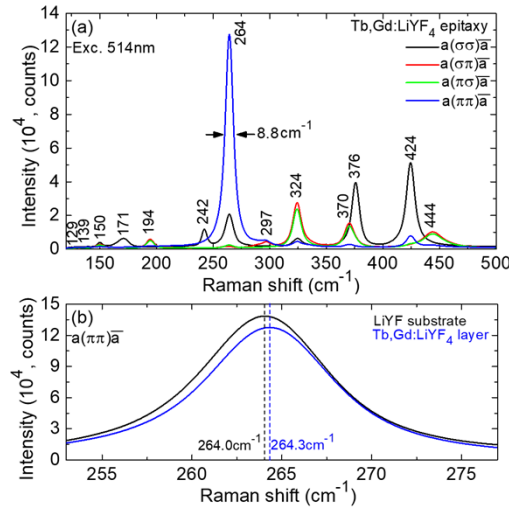


**Fig. 7.** (a) Polarized  $\mu$ -Raman spectra of the Tb,Gd:LiYF<sub>4</sub> epitaxial layer in the  $a(ij)a$  geometry ( $i, j = \pi, \sigma$ ), (b) a close look at the most intense Raman peak at  $\sim 264\ \text{cm}^{-1}$  for the substrate and the layer in the  $a(\pi\pi)a$  geometry,  $\lambda_{\text{exc}} = 514\ \text{nm}$ .

A slight blue-shift of  $0.3\ \text{cm}^{-1}$  is visible in the peak position of the band at  $\sim 264\ \text{cm}^{-1}$  between the Raman spectra of the LiYF<sub>4</sub> substrate and the Tb,Gd:LiYF<sub>4</sub> layer, Fig. 7(b), for the  $a(\pi\pi)a$  configuration. This phenomenon is due to the variation of the crystalline structure generated by the Tb<sup>3+</sup> and Gd<sup>3+</sup> doping of the layer. The Raman peak for the layer is also slightly broadened and reduced in intensity as compared to that of the substrate indicating only a slight reduction in crystallinity as compared to the undoped single-crystal.

The well-preserved polarization anisotropy of the Raman spectra of the epitaxial layer indicates the conservation of its orientation with respect to the substrate (*i.e.*, growth along the [001] crystallographic direction).

### 4.4. Optical spectroscopy

The excitation spectrum of Tb<sup>3+</sup> ions in the epitaxial layer is shown in Fig. 8, when monitoring the green emission at 544 nm. The most intense band in the UV spectral range at  $\sim 375.9\ \text{nm}$  is due to the  $^7F_6 \rightarrow ^5D_3$  transition. The transition to the metastable  $^5D_4$  Tb<sup>3+</sup> level corresponds to a band falling in the blue spectral range with a maximum at 488 nm, which is commonly used for pumping Tb lasers. The spectrally overlapping bands in the UV are due to transitions to the higher-lying  $^5G_J$ ,  $^5D_J$ ,  $^5L_J$ ,  $^5H_J$  multiplets of Tb<sup>3+</sup> ions. Here, the assignment of the spectral bands was made according to Carnall *et al.* [36].



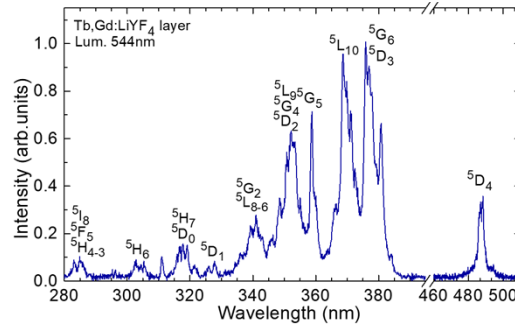


**Fig. 8.** Excitation spectrum of  $\text{Tb}^{3+}$  ions in the  $\text{Tb,Gd:LiYF}_4$  epitaxial layer,  $\lambda_{\text{lum}} = 544$  nm.

The tetragonal  $\text{LiYF}_4$  crystal is optically uniaxial and its optical axis is parallel to the  $c$ -axis. Two principal light polarizations are denoted  $\pi$  ( $E \parallel c$ ) and  $\sigma$  ( $E \perp c$ ). The polarized luminescence spectra of  $\text{Tb}^{3+}$  ions in the epitaxial layer are shown in Fig. 9(a). The highest luminescence intensity is observed for  $\pi$ -polarization, for all the  $^5\text{D}_4 \rightarrow ^7\text{F}_J$  transitions ( $J = 0-6$ ). The most intense emission is related to the  $^5\text{D}_4 \rightarrow ^7\text{F}_5$  transition between 539 and 555 nm, responsible for the green luminescence of  $\text{Tb}^{3+}$  ions. The CIE 1931 (*Commission internationale de l'éclairage*) colour coordinates for the luminescence of the  $\text{Tb,Gd:LiYF}_4$  epitaxial layer are  $x = 0.331$  and  $y = 0.591$  falling into the green spectral range. The dominant wavelength  $\lambda_d$  is 553.9 nm with colour purity  $p = 77.5\%$ .

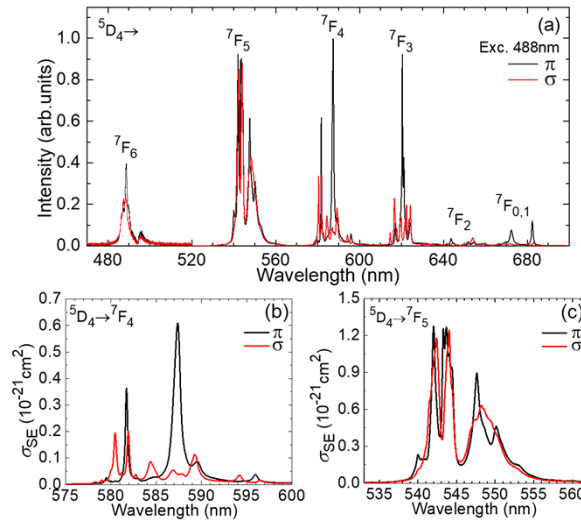


**Fig. 9.** (a) Polarized luminescence spectra of  $\text{Tb}^{3+}$  ions in the  $\text{Tb,Gd:LiYF}_4$  epitaxial layer for  $\pi$  and  $\sigma$  light polarizations,  $\lambda_{\text{exc}} = 488$  nm; (b,c) stimulated-emission cross-sections for  $\text{Tb}^{3+}$  ions: (b) the  $^5\text{D}_4 \rightarrow ^7\text{F}_4$  transition (yellow emission) and (c) the  $^5\text{D}_4 \rightarrow ^7\text{F}_5$  transition (green emission).

The peak wavelengths of all the  $^5\text{D}_4 \rightarrow ^7\text{F}_J$   $\text{Tb}^{3+}$  emission bands in the epitaxial layer are listed in Table 1, together with the corresponding colours.  $\text{Tb}^{3+}$  ions provide multi-colour emission falling into the blue ( $J = 6$ ), green ( $J = 5$ ), yellow ( $J = 4$ ), red ( $J = 2, 3$ ) and deep-red ( $J = 0, 1$ ) spectral ranges. The experimental luminescence branching ratios  $B_{\text{exp}}(\text{JJ}')$  were calculated from the unpolarized luminescence spectra by integrating the luminescence intensity for each transition.

The highest  $B_{\text{exp}}(JJ')$  of 53.76% corresponds to the most intense  $^5D_4 \rightarrow ^7F_5$  transition. This value agrees with those reported previously for a  $\text{LiTbF}_4$  stoichiometric crystal: 58.9% (experimental) and 58.18% (calculated using the Judd-Ofelt theory [27]). The  $^5D_4 \rightarrow ^7F_4$  transition falling in the yellow spectral range corresponds to a smaller  $B_{\text{exp}}(JJ')$  of 10.58%.

**Table 1. Luminescence Branching Ratios for the  $^5D_4 \rightarrow ^7F_J$  ( $J = 0 - 6$ ) Transitions of  $\text{Tb}^{3+}$  Ions in the  $\text{Tb,Gd:LiYF}_4$  Epitaxial Layer**

Transition $^5D_4 \rightarrow ^7F_J$	$\lambda_{\text{em}}$ , nm This work	$B_{\text{exp}}(JJ')$ , % This work	$B_{\text{exp}}(JJ')$ , % <sup>a</sup> [27]	$B_{\text{calc}}(JJ')$ , % <sup>a</sup> [27]	Emission color
$^7F_6$	489	28.73	16.49	8.46	Blue
$^7F_5$	544	53.76	58.9	58.18	Green
$^7F_4$	587	10.58	13.58	6.27	Yellow
$^7F_3$	620	4.93	8.632	19.75	Red
$^7F_2$	654	1.18	1.18	1.98	Red
$^7F_1$	672	0.651	0.748	2.91	Deep-red
$^7F_0$	683	0.223	0.47	2.44	Deep-red

<sup>a</sup>The experimental and calculated  $B(JJ')$  values for a stoichiometric crystal  $\text{LiTbF}_4$  are given for comparison.

The micro-luminescence mapping was performed across the polished end-facet of the epitaxy, as shown in Fig. 10. The  $\text{Tb}^{3+}$  ions are only located in the layer, with a slight increase in concentration towards the surface of the layer, and no  $\text{Tb}^{3+}$  diffusion into the substrate is observed.

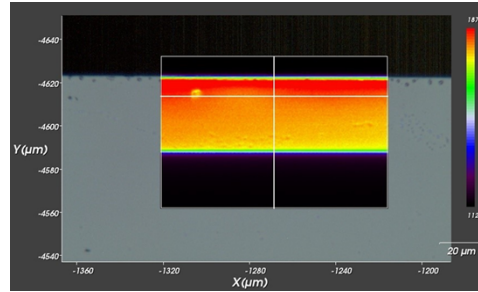


**Fig. 10.** Micro-luminescence mapping across a polished end-facet of a  $\text{Tb,Gd:LiYF}_4$  /  $\text{LiYF}_4$  epitaxy,  $\lambda_{\text{exc}} = 488$  nm,  $\lambda_{\text{lum}} = 544$  nm.

Polarized stimulated-emission (SE) cross-section,  $\sigma_{\text{SE}}$ , spectra for the  $^5D_4 \rightarrow ^7F_{4,5}$  transitions were calculated from the corresponding polarized luminescence spectra using the Füchtbauer-Ladenburg (F-L) equation [37]:

$$\sigma_{\text{SE}}^i(\lambda) = \frac{\lambda^5}{8\pi \langle n \rangle^2 \tau_{\text{rad}} c} \cdot \frac{B_{\text{exp}}(JJ') \cdot W_i(\lambda)}{\frac{1}{3} \sum_{i=2\sigma, \pi} \int \lambda W_i(\lambda) d\lambda}, \quad (1)$$

where  $W_i(\lambda)$  the luminescence spectrum for each light polarization ( $i = \sigma, \pi$ ),  $\langle n \rangle$  the average refractive index at the mean emission wavelength,  $\tau_{\text{rad}}$  the radiative lifetime of the emitting state ( $^5D_4$ ), and  $B_{\text{exp}}(JJ')$  the luminescence branching ratio. The results are shown in Fig. 9(b,c). The  $\text{Tb}^{3+}$  ions in the epitaxial layer exhibit strong polarization anisotropy of the SE cross-sections for both considered transitions, being more pronounced for the  $^5D_4 \rightarrow ^7F_4$  transition, with the maximum  $\sigma_{\text{SE}}$  values obtained for  $\pi$ -polarization. This is a prerequisite for linearly polarized emission in lasers.

For the  $^5D_4 \rightarrow ^7F_4$  transition in the yellow, the maximum SE cross-section is  $0.61 \times 10^{-21} \text{ cm}^2$  at 587.4 nm (for  $\pi$ -polarization) and  $0.20 \times 10^{-21} \text{ cm}^2$  at 581.9 nm (for  $\sigma$ -polarization). For the

$^5D_4 \rightarrow ^7F_5$  transition in the green, the corresponding values are higher,  $1.28 \times 10^{-21} \text{ cm}^2$  at 542.0 nm (for  $\pi$ -polarization) and  $1.25 \times 10^{-21} \text{ cm}^2$  at 544.0 nm (for  $\sigma$ -polarization).

The luminescence decay curves for  $\text{Tb}^{3+}$  ions in the epitaxial layer at both RT and LT (12 K) are shown in Fig. 11(a), observing the green emission ( $\sim 544 \text{ nm}$ ). The decay curves are single-exponential, in agreement with a single rare-earth site in  $\text{LiYF}_4$  ( $\text{Y}^{3+}$  ions,  $S_4$  symmetry, VIII-fold  $F^-$  coordination). The luminescence lifetime  $\tau_{\text{lum}}$  of the  $^5D_4$   $\text{Tb}^{3+}$  state is 5.05 ms (at RT) and 5.41 ms (at 12 K).

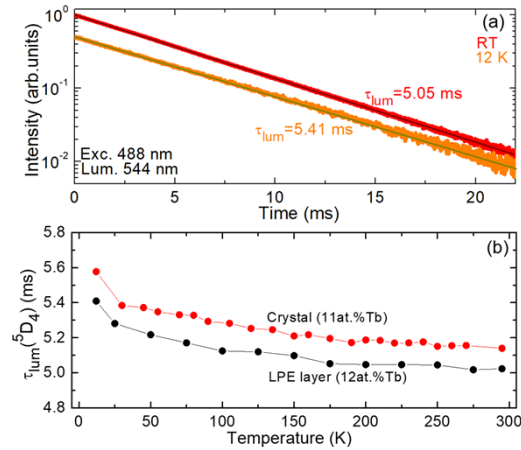


**Fig. 11.** (a) Luminescence decay curves from the  $^5D_4$  state of  $\text{Tb}^{3+}$  ions in the  $\text{Tb,Gd:LiYF}_4$  epitaxial layer at 12 K and RT (black and green lines – single-exponential fits); (b) the luminescence lifetimes of the  $^5D_4$  state as a function of temperature, the data for a 11 at.%  $\text{Tb:LiYF}_4$  crystal are given for comparison.

The luminescence lifetime of the  $^5D_4$   $\text{Tb}^{3+}$  state was also measured as a function of temperature, from 12 to 295 K, for both the 12 at.% Tb, 5 at.%  $\text{Gd:LiYF}_4$  epitaxial layer and a 11.2 at.%  $\text{Tb:LiYF}_4$  single-crystal studied for comparison, see Fig. 11(b). The  $\tau_{\text{lum}}$  value slightly increases upon cooling for both samples and it is only slightly longer for the single-crystal, 5.14 ms (at RT) and 5.58 ms (at 12 K). The latter indicates a relatively low content of quenching centers (defects and impurities) in the epitaxial layer highlighting its good optical quality.

#### 4.5. Low-temperature spectroscopy

The crystal-field splitting for  $\text{Tb}^{3+}$  multiplets in the  $\text{Tb,Gd:LiYF}_4$  epitaxial layer was determined from the LT (12 K) excitation and luminescence spectra, Fig. 12(a-e). The LT luminescence spectra corresponding to all the  $^5D_4 \rightarrow ^7F_J$  ( $J = 0-6$ ) transitions were measured under excitation at 375 nm (to the higher-lying  $^5G_6 + ^5D_3$  states). They were plotted vs.  $E_{\text{ZPL}} - E_{\text{ph}}$ , where  $E_{\text{ZPL}}$  is the zero-phonon line (ZPL) energy for transitions between the lowest Stark sub-levels of the metastable state  $^5D_4$  and the ground-state  $^7F_6$ , and  $E_{\text{ph}}$  is the photon energy, thus directly giving the experimental energy of each Stark sub-levels of the  $^7F_J$  multiplets. The excitation spectrum corresponding to the  $^7F_6 \rightarrow ^5D_4$  transition was measured when monitoring the green emission at 542 nm and it was plotted vs.  $E_{\text{ph}}$ , directly giving the experimental energy of each Stark sub-level for the  $^5D_4$  metastable state.

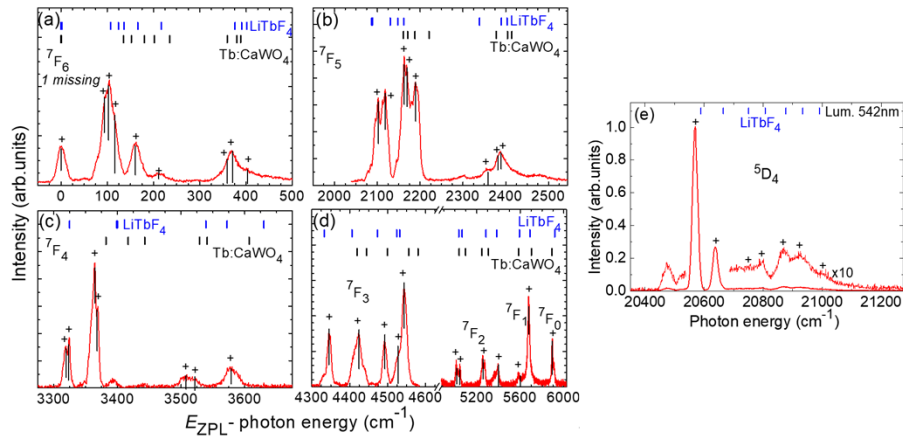


**Fig. 12.** LT (12 K) spectroscopic studies of  $\text{Tb}^{3+}$  ions in the  $\text{Tb,Gd:LiYF}_4$  epitaxial layer: (a-d) luminescence spectra,  $\lambda_{\text{exc}} = 375$  nm, (e) excitation spectrum,  $\lambda_{\text{lum}} = 542$  nm. Vertical dashes – crystal-field splitting for  $\text{Tb}^{3+}$  ions in tetragonal  $\text{LiTbF}_4$  and  $\text{CaWO}_4$  crystals (after [33,34]).

For  $\text{Tb}^{3+}$  ions residing in  $S_4$  symmetry sites, any  $^{2S+1}L_J$  multiplet with a total angular momentum  $J$  of 0, 1, 2, 3, 4, 5 and 6, will be split into a total of 1, 2, 4, 5, 7, 8 and 10 Stark sub-levels, respectively. The assignment of the electronic transitions in the LT excitation and luminescence spectra (indicated by the “+” symbols) was performed following the previous studies on the crystal-field splitting of  $\text{Tb}^{3+}$  ions in isostructural (scheelite-type)  $\text{LiTbF}_4$  [38] and  $\text{CaWO}_4$  [39] crystals. The experimental energies of Stark sub-levels are listed in Table 2, together with the expected number of sub-levels according to Christensen [38]. Only one experimental sub-level of the  $^7F_6$  multiplet is missing from the LT luminescence spectrum.

**Table 2. Experimental Crystal-Field Splitting of the  $^7F_J$  ( $J = 0 - 6$ ) and  $^5D_4$   $\text{Tb}^{3+}$  Multiplets in the  $\text{Tb,Gd:LiYF}_4$  Epitaxial Layers**

Level	Expected number of sub-levels ( $S_4$ sites)	Experimental energies ( $\text{cm}^{-1}$ )
$^7F_6$	10	0, 93, 103, 116, 160, 211, 359, 370, 402 (1 missing)
$^7F_5$	8	2102, 2118, 2163, 2169, 2190, 2358, 2381, 2389
$^7F_4$	7	3319, 3323, 3364, 3368, 3508, 3521, 3578
$^7F_3$	5	4345, 4424, 4493, 4528, 4544
$^7F_2$	4	5020, 5043, 5261, 5398
$^7F_1$	2	5600, 5673
$^7F_0$	1	5891
$^5D_4$	7	20569, 20638, 20749, 20797, 20870, 20923, 21003

The experimental Stark sub-level energies were used to plot the  $\text{Tb}^{3+}$  energy-level diagram in  $\text{Tb,Gd:LiYF}_4$  epitaxial layers, Fig. 13, also showing the multi-colour  $^5D_4 \rightarrow ^7F_J$  ( $J = 0 - 6$ ) emissions falling into the blue, green, yellow, red and deep-red spectral ranges.

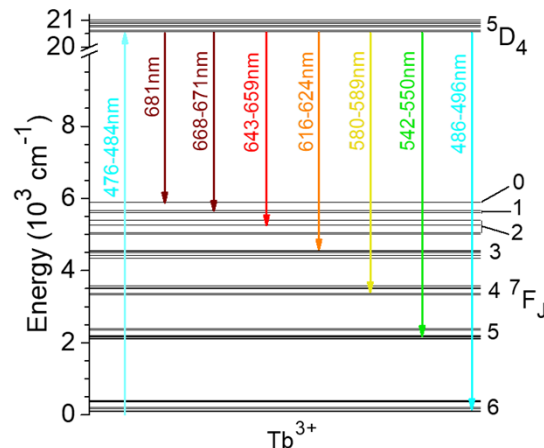


**Fig. 13.** Energy-level scheme of  $\text{Tb}^{3+}$  ions in the  $\text{Tb,Gd:LiYF}_4$  epitaxial layer, arrows indicate the transitions corresponding to visible absorption / emissions to / from the  $^5\text{D}_4$  metastable state.

## 5. Conclusion

We demonstrate the suitability of Liquid Phase Epitaxy for the growth of heavily  $\text{Tb}^{3+}$ -doped single-crystalline oriented  $\text{LiYF}_4$  layers with a thickness of a few tens of  $\mu\text{m}$  on bulk undoped  $\text{LiYF}_4$  substrates. A starting layer composition of  $\text{LiY}_{0.83}\text{Tb}_{0.12}\text{Gd}_{0.05}\text{F}_4$  was tested (with  $\text{Tb}^{3+}$  ions being the active centers and  $\text{Gd}^{3+}$  ones serving for increasing the refractive index contrast between the layer and the substrate). The layers exhibit (i) a single-crystalline structure without cracks and impurities and a clean and planar layer / substrate interface, (ii) a well-preserved orientation with respect to the substrate (growth along the [001] direction), (iii) a uniform distribution of  $\text{Tb}^{3+}$  ions with no diffusion into the substrate, (iv) strongly polarized emission properties and (v) a long lifetime of the metastable  $^5\text{D}_4$   $\text{Tb}^{3+}$  level. We also report on key spectroscopic parameters of  $\text{Tb}^{3+}$  ions in  $\text{Tb,Gd:LiYF}_4$  epitaxial layers being relevant for laser operation, such as the polarized stimulated-emission cross-sections for green and yellow  $\text{Tb}^{3+}$  emissions, the luminescence branching ratios, the radiative  $\text{Tb}^{3+}$  lifetime and the crystal-field splitting. The developed epitaxies are promising for visible (green and yellow) waveguide lasers.

Future work will focus on the LPE growth of epitaxial layers with yet higher  $\text{Tb}^{3+}$  doping levels, up to the stoichiometric composition  $\text{LiTbF}_4$ , with the goal of increasing the light absorption in the blue and UV spectral ranges limited by the low probabilities of the corresponding spin-forbidden  $\text{Tb}^{3+}$  transitions. The growth of stoichiometric epitaxial layers on top of a  $\text{LiYF}_4$  substrate should theoretically lead to a lattice mismatch of  $\Delta a/a_{\text{substrate}} = 0.69\%$  and  $\Delta c/c_{\text{substrate}} = 1.28\%$ .

**Funding.** Agence Nationale de la Recherche (ANR-22-CE08-0025-01, NOVELA); European Regional Development Fund; Contrat de plan État-Région (CPER) de Normandie; Agencia Estatal de Investigación (PID2019-108543RB-I00).

**Disclosures.** The authors declare no conflicts of interest.

**Data availability.** Data underlying the results presented in this paper are not publicly available at this time but may be obtained from the authors upon reasonable request.

## References

1. C. Kränkel, D.-T. Marzahl, F. Moglia, G. Huber, and P. W. Metz, "Out of the blue: semiconductor laser pumped visible rare-earth doped lasers," *Laser Photonics Rev.* **10**(4), 548–568 (2016).
2. P. W. Metz, D.-T. Marzahl, A. Majid, C. Kränkel, and G. Huber, "Efficient continuous wave laser operation of  $\text{Tb}^{3+}$ -doped fluoride crystals in the green and yellow spectral regions," *Laser Photonics Rev.* **10**(2), 335–344 (2016).
3. S. Kalusniak, H. Tanaka, E. Castellano-Hernández, and C. Kränkel, "UV-pumped visible  $\text{Tb}^{3+}$ -lasers," *Opt. Lett.* **45**(22), 6170–6173 (2020).

4. R. P. Rao, "Tb<sup>3+</sup> activated green phosphors for plasma display panel applications," *J. Electrochem. Soc.* **150**(8), H165–H171 (2003).
5. Z. Xia and R. S. Liu, "Tunable blue-green color emission and energy transfer of Ca<sub>2</sub>Al<sub>3</sub>O<sub>6</sub>F:Ce<sup>3+</sup>, Tb<sup>3+</sup> phosphors for near-UV white LEDs," *J. Phys. Chem. C* **116**(29), 15604–15609 (2012).
6. Y. Zhai, Q. Sun, S. Yang, Y. Liu, J. Wang, S. Ren, and S. Ding, "Morphology-controlled synthesis and luminescence properties of green-emitting NaGd(WO<sub>4</sub>)<sub>2</sub>:Tb<sup>3+</sup> phosphors excited by n-UV excitation," *J. Alloys Compd.* **781**, 415–424 (2019).
7. U. Yadav, Z. Abbas, R. J. Butcher, and A. K. Patra, "A luminescent terbium (III) probe as an efficient turn-on sensor for dipicolinic acid, a bacillus anthracis biomarker," *New J. Chem.* **46**(38), 18285–18294 (2022).
8. A. Mohammadzadeh, A. Jouyban, M. Hasanzadeh, V. Shafiei-Irannejad, and J. Soleymani, "Ultrasensitive fluorescence detection of antitumor drug methotrexate based on a terbium-doped silica dendritic probe," *Anal. Methods* **13**(37), 4280–4289 (2021).
9. V. Vasyliiev, E. G. Villora, M. Nakamura, Y. Sugahara, and K. Shimamura, "UV-visible Faraday rotators based on rare-earth fluoride single crystals: LiREF<sub>4</sub> (RE = Tb, Dy, Ho, Er and Yb), PrF<sub>3</sub> and CeF<sub>3</sub>," *Opt. Express* **20**(13), 14460–14470 (2012).
10. X. Xin, Y. Hao, L. Liu, J. Lv, J. Zhang, X. Fu, Z. Jia, and X. Tao, "Tb<sub>3</sub>Al<sub>3</sub>Ga<sub>2</sub>O<sub>12</sub>: A novel visible–infrared Faraday crystal exhibiting a superior magneto-optical performance," *Cryst. Growth Des.* **22**(9), 5535–5541 (2022).
11. R. K. Verma, K. Kumar, and S. B. Rai, "Inter-conversion of Tb<sup>3+</sup> and Tb<sup>4+</sup> states and its fluorescence properties in MO–Al<sub>2</sub>O<sub>3</sub>:Tb (M = Mg, Ca, Sr, Ba) phosphor materials," *Solid State Sci.* **12**(7), 1146–1151 (2010).
12. J. Kaszewski, B. S. Witkowski, Ł. Wachnicki, H. Przybylińska, B. Kozankiewicz, E. Mijowska, and M. Godlewski, "Reduction of Tb<sup>4+</sup> ions in luminescent Y<sub>2</sub>O<sub>3</sub>:Tb nanorods prepared by microwave hydrothermal method," *J. Rare Earths* **34**(8), 774–781 (2016).
13. M. F. Churbanov, B. I. Denker, B. I. Galagan, V. V. Koltashev, V. G. Plotnichenko, M. V. Sukhanov, S. E. Sverchkov, and A. P. Velmuzhov, "First demonstration of ~5 μm laser action in terbium-doped selenide glass," *Appl. Phys. B* **126**(7), 117 (2020).
14. V. S. Shiryayev, M. V. Sukhanov, A. P. Velmuzhov, E. V. Karaksina, T. V. Kotereva, G. E. Snopatin, B. I. Denker, B. I. Galagan, S. E. Sverchkov, V. V. Koltashev, and V. G. Plotnichenko, "Core-clad terbium doped chalcogenide glass fiber with laser action at 5.38 μm," *J. Non-Cryst. Solids* **567**, 120939 (2021).
15. S. Kalusniak, E. Castellano-Hernández, H. Yalçinoğlu, H. Tanaka, and C. Kränkel, "Spectroscopic properties of Tb<sup>3+</sup> as an ion for visible lasers," *Appl. Phys. B* **128**(2), 33 (2022).
16. P. W. Metz, D.-T. Marzahl, G. Huber, and C. Kränkel, "Performance and wavelength tuning of green emitting terbium lasers," *Opt. Express* **25**(5), 5716–5724 (2017).
17. E. Castellano-Hernández, P. W. Metz, M. Demesh, and C. Kränkel, "Efficient directly emitting high-power Tb<sup>3+</sup>:LiLuF<sub>4</sub> laser operating at 587.5 nm in the yellow range," *Opt. Lett.* **43**(19), 4791–4794 (2018).
18. T. Yamashita and Y. Ohishi, "Amplification and lasing characteristics of Tb<sup>3+</sup>-doped fluoride fiber in the 0.54 μm band," *Jpn. J. Appl. Phys.* **46**(No. 41), L991–L993 (2007).
19. V. Vasyliiev, E. G. Villora, Y. Sugahara, and K. Shimamura, "Judd-Ofelt analysis and emission quantum efficiency of Tb-fluoride single crystals: LiTbF<sub>4</sub> and Tb<sub>0.81</sub>Ca<sub>0.19</sub>F<sub>2.81</sub>," *J. Appl. Phys.* **113**(20), 203508 (2013).
20. B. Ferrand, B. Chambaz, and M. Couchaud, "Liquid phase epitaxy: A versatile technique for the development of miniature optical components in single crystal dielectric media," *Opt. Mater.* **11**(2-3), 101–114 (1999).
21. P. Rogin and J. Hulliger, "Liquid phase epitaxy of LiYF<sub>4</sub>," *J. Cryst. Growth* **179**(3-4), 551–558 (1997).
22. P. Loiko, R. Soular, G. Brasse, J.-L. Doualan, B. Guichardaz, A. Braud, A. Tyazhev, A. Hideur, and P. Camy, "Watt-level Tm:LiYF<sub>4</sub> channel waveguide laser produced by diamond saw dicing," *Opt. Express* **26**(19), 24653–24662 (2018).
23. L. Basyrova, G. Brasse, P. Loiko, C. Grygiel, R. M. Solé, M. Aguiló, F. Díaz, X. Mateos, A. Benayad, J.-L. Doualan, and P. Camy, "Liquid phase epitaxy growth and structural characterization of highly-doped Er<sup>3+</sup>:LiYF<sub>4</sub> thin films," *Opt. Mater.* **132**, 112574 (2022).
24. W. Bolaños, F. Starecki, A. Braud, J.-L. Doualan, R. Moncorgé, and P. Camy, "2.8 W end-pumped Yb<sup>3+</sup>:LiYF<sub>4</sub> waveguide laser," *Opt. Lett.* **38**(24), 5377–5380 (2013).
25. P. Loiko, R. Soular, G. Brasse, J.-L. Doualan, A. Braud, A. Tyazhev, A. Hideur, and P. Camy, "Tm,Ho:LiYF<sub>4</sub> planar waveguide laser at 2.05 μm," *Opt. Lett.* **43**(18), 4341–4344 (2018).
26. W. Bolaños, G. Brasse, F. Starecki, A. Braud, J.-L. Doualan, R. Moncorgé, and P. Camy, "Green, orange, and red Pr<sup>3+</sup>:YLiF<sub>4</sub> epitaxial waveguide lasers," *Opt. Lett.* **39**(15), 4450–4453 (2014).
27. G. Brasse, P. Loiko, C. Grygiel, A. Benayad, F. Lemarie, V. Zakharov, A. Veniaminov, J.-L. Doualan, A. Braud, and P. Camy, "Liquid Phase Epitaxy growth, structure and spectroscopy of highly-doped 20 at.% Yb<sup>3+</sup>:LiYF<sub>4</sub> thin films," *J. Lumin.* **236**, 118071 (2021).
28. R. Soular, M. Salhi, G. Brasse, P. Loiko, J.-L. Doualan, A. Braud, A. Tyazhev, A. Hideur, and P. Camy, "Laser operation of highly-doped Tm:LiYF<sub>4</sub> epitaxies: Towards thin-disk lasers," *Opt. Express* **27**(6), 9287–9301 (2019).
29. R. E. Thoma, C. F. Weaver, H. A. Freidman, H. Insley, L. A. Harris, and H. A. Yakel, "Phase equilibria in the system LiF–YF<sub>3</sub>," *J. Phys. Chem.* **65**(7), 1096–1099 (1961).
30. P. P. Fedorov, B. P. Sobolev, L. V. Medvedeva, and B. M. Reiterov, "Revised phase diagrams of LiF–RF<sub>3</sub> (R = La – Lu, Y) systems," in *Growth of Crystals*, vol. 21 E. I. Givargizov and A. M. Mel'nikova, eds., (Springer US, 2002), pp. 141–154.



31. A. A. Kaminskii, *Laser Crystals*, vol. 14 Springer Series in Optical Sciences (Springer Berlin Heidelberg, 1990).
32. E. García and R. R. Ryan, "Structure of the laser host material  $\text{LiYF}_4$ ," *Acta Crystallogr., Sect. C: Cryst. Struct. Commun.* **49**(12), 2053–2054 (1993).
33. A. Grzechnik, W. A. Crichton, P. Bouvier, V. Dmitriev, H.-P. Weber, and J.-Y. Gesland, "Decomposition of  $\text{LiGdF}_4$  scheelite at high pressures," *J. Phys.: Condens. Matter* **16**(43), 7779–7786 (2004).
34. T. C. Damen, S. P. S. Porto, and B. Tell, "Raman effect in zinc oxide," *Phys. Rev.* **142**(2), 570–574 (1966).
35. S. A. Miller, H. E. Rast, and H. H. Caspers, "Lattice vibrations of  $\text{LiYF}_4$ ," *J. Chem. Phys.* **52**(8), 4172–4175 (1970).
36. W. T. Carnall, P. R. Fields, and K. Rajnak, "Electronic energy levels of the trivalent lanthanide aquo ions. III.  $\text{Tb}^{3+}$ ," *J. Chem. Phys.* **49**(10), 4447–4449 (1968).
37. B. Aull and H. Jenssen, "Vibronic interactions in Nd:YAG resulting in nonreciprocity of absorption and stimulated emission cross sections," *IEEE J. Quantum Electron.* **18**(5), 925–930 (1982).
38. H. P. Christensen, "Spectroscopic analysis of lithium terbium tetrafluoride," *Phys. Rev. B* **17**(10), 4060–4068 (1978).
39. R. P. Leavitt, C. A. Morrison, and D. E. Wortman, "Description of the crystal field for  $\text{Tb}^{3+}$  in  $\text{CaWO}_4$ ," *J. Chem. Phys.* **61**(3), 1250–1251 (1974).